



Modulation of Turbulence Flux Budgets by Varying Fluid Properties in Heated High Prandtl Number Flow

Christoph Irrenfried¹ · Helfried Steiner¹

Received: 16 May 2023 / Accepted: 10 August 2023 / Published online: 5 September 2023
© The Author(s) 2023

Abstract

The accurate computational modelling of momentum and heat transfer in turbulent wall-bounded flow is still a challenging task, especially for fluids with high molecular Prandtl numbers. Due to the steep temperature gradients, the strong variation of fluid properties becomes an additional important issue. The present Direct Numerical Simulation study specially addresses this problem considering a representative working fluid in terms of a real heat transfer oil with temperature-dependent material properties. Near the heated wall, the increase in molecular viscosity significantly attenuates the turbulent convective fluxes of both momentum and heat, despite the markedly increased enthalpy fluctuations. As the thermal conductivity decreases markedly less with temperature than the viscosity, the dampened turbulent mixing significantly reduces the Nusselt number, whereas the skin friction coefficient only marginally differs from the constant fluid property case. The attenuation of the radial velocity fluctuation consistently reduces the production terms in the budgets of the turbulent momentum and heat fluxes, while the production of the enthalpy fluctuations is only shifted away from the wall without significant change in peak level. The also attenuated redistribution in the turbulent axial stress budget reduces the pressure-strain based steering of turbulence towards isotropy. Facing a consequently more anisotropic turbulent motion poses a further difficulty to standard turbulence modelling mostly developed for isotropic turbulence.

Keywords High Prandtl number liquids · Direct Numerical Simulation · Material property variation · Turbulence budgets

List of Symbols

C_f Skin friction coefficient (–)
 C_{nm}^* Mean convection tensor (–)

Christoph Irrenfried and Helfried Steiner contributed equally to this work.

✉ Helfried Steiner
helfried.steiner@tugraz.at

Christoph Irrenfried
c.irrenfried@tugraz.at

¹ Institute of Fluid Mechanics and Heat Transfer, Graz University of Technology, Inffeldgasse 25F, 8010 Graz, Styria, Austria

c_p	Specific heat capacity (J/kgK)
D	Pipe diameter (m)
D_{nm}^*	Viscous diffusion tensor (–)
\mathbf{f}_w	Sourceterm in momentum equation enforcing axial periodicity (–)
f_χ	Sourceterm in energy equation enforcing axial periodicity (–)
h	Specific enthalpy (J/kg)
h_τ	Specific wall friction enthalpy (J/kg)
P	Pressure (Pa)
P_{nm}^*	Rate of production tensor (–)
q_m	Heat flux vector (W/m ²)
q_w	Wall heat flux (W/m ²)
\dot{m}	Mass flow rate (kg/s)
$r, r\varphi, z$	Radial, azimuthal and axial coordinates (m)
\underline{S}	Rate of strain tensor (1/s)
t	Time (s)
T	Temperature (K)
T_{nm}^*	Turbulent diffusion tensor (–)
$\mathbf{U} = (u, v, w)^T$	Velocity vector in radial, azimuthal, axial direction (m/s)
w_τ	Wall friction velocity (m/s)
ϵ	Averaged dissipation rate (m ² /s ³)
ϵ_{nm}^*	Dissipation tensor (–)
η	Kolmogorov micro length scale (m)
η_θ	Batchelor micro length scale (m)
λ	Thermal conductivity (W/mK)
μ	Dynamic viscosity (Pas)
ν	Kinematic viscosity (m ² /s)
Π_{mn}^*	Velocity pressure-gradient tensor (–)
ρ	Density (kg/m ³)
τ	Shear stress (Pa)
τ_{mn}	Viscous stress tensor (Pa)
$\chi = h - h_w$	Specific enthalpy difference to the wall value (J/kg)
Nu	Nusselt number (–)
Pr	Molecular Prandtl number (–)
Ra	Rayleigh number (–)
Re	Reynolds number (–)
Ri	Richardson number (–)
Sc	Schmidt number (–)

Subscripts and Superscripts

b	Bulk
CFP	Constant fluid properties
lam	Laminar
tot	Total
$turb$	Turbulent
τ	Friction
VFP	Variable fluid properties
w	Wall
$()^*$	Non-dimensionalized

$()^+$	Representation in wall-units
$()'$	Fluctuation relative to Reynolds average
$\langle \rangle$	Reynolds average

1 Introduction

High Prandtl number liquids are most commonly used for lubrication and cooling of various industrial engineering applications. The large disparity of the smallest turbulent dynamic and thermal scales strongly challenges the computational modeling of the transport of momentum and heat. With increasing molecular Prandtl number, the thermal resistance of the near wall layer increases, so that essential heat transfer related thermo-physical phenomena are shifted closer to the wall. The associated steeper temperature gradients generally lead to a marked variation of the fluid properties. The commonly assumed neglect of this variation may significantly add to predictive uncertainty.

For a reliable description and ultimately adequate computational modelling of momentum and energy transfer with significant material property variation, a detailed understanding of the underlying transport processes in the near wall layer is necessary. The required highly accurate and comprehensive insight can be basically provided best by the computational method of Direct Numerical Simulation (DNS), which by definition attempts to capture numerically all relevant dynamic and thermal small scale structures occurring in the near wall layer.

For unheated isothermal conditions, there exists a meanwhile very rich literature on DNS of fully developed channel and pipe flow. Among these, we exemplarily mention the studies of Wu and Moin (2008), Boersma (2011), who carried out highly resolved DNS for unheated pipe flow giving a detailed analysis of the first and second-order turbulence moments. Regarding DNS with heat transfer, the majority considered low molecular Prandtl numbers, around unity as representative for gases, and constant material properties, such as the work of Kim and Moin (1987), Piller (2005), Kawamura et al. (1998), Redjem-Saad et al. (2007). Considering conditions more relevant to liquids, Na and Hanratty (2000), Kozuka et al. (2009) investigated higher-order turbulence statistics for turbulent channel flow at molecular Prandtl numbers up to $Pr = 10$. The DNS of Tiselj et al. (2001) considered planar channel flow at $Pr = 7$ including conjugate heat transfer in the solid wall. Equivalent to the heat transfer simulations for high Prandtl numbers, Schwertfirm and Manhart (2007) presented DNS simulations with passive scalar transport in a turbulent channel for very high Schmidt numbers up to $Sc = 49$.

Comparatively few DNS with Prandtl numbers beyond unity thus far considered temperature-dependent material properties, being focussed in the present work. Among these previous studies, Lee et al. (2013) investigated the influence of wall heating on the skin friction coefficient by performing DNS of turbulent boundary layers with temperature-dependent viscosity at a Prandtl number $Pr = 5.4$. Zonta et al. (2012) investigated the effect of temperature-dependent viscosity on forced convection in a channel flow with a heated and a cooled wall for $Pr = 3$, illustrating in particular the effect of the low viscosity region near the hot side of the channel. The effect of varying density due to volumetric dilatation was investigated by various incompressible DNS applying Boussinesqu's approximation. Dependent on the wall normal change in density, buoyancy forces may foster stably or unstably stratified flow conditions, where turbulent advective transport is basically dampened or enhanced, respectively. García-Villalba and Álamo (2011) examined

stably stratified planar channel flow for increasing friction Richardson numbers Ri_τ up to the limit of relaminarization, where the inner core-flow region turned out as most strongly affected by buoyancy, while the near wall region essentially resembled the neutral case. Computational as well as experimental issues typically met with stably stratified flow were addressed in the review of Zonta and Soldati (2018). The DNS of Scagliarini et al. (2015) investigated unstably stratified channel flow at moderate friction Reynolds numbers up to $Re_\tau = 205$ showing markedly enhanced wall normal velocity fluctuations for Rayleigh numbers above $Ra \approx 10^6$, while insignificantly little effect of buoyancy was seen below. Patel et al. (2015) considered strongly compressible flow associated with high variations in density caused by substantial changes in thermodynamic pressure. It was shown, that introducing a semi-local scaling makes the turbulent velocity statistics obtained for varying fluid properties effectively collapse with corresponding constant property results. Later, Patel et al. (2017) proposed a similar scaling approach for a universal description of the temperature. The DNS of Nemati et al. (2016) considered heated turbulent pipe flow at super-critical pressure facing very peculiar non-monotonous material property variations. They observed a notable deterioration in heat transfer caused by these variations.

Most of the more recent highly resolved DNS rather focussed the effect of increasing Reynolds number, while assuming Prandtl number not far beyond unity and constant fluid properties (Alcántara-Ávila et al. 2021; Moser et al. 1999; Pirozzoli et al. 2022; Hoyas et al. 2022; Yao et al. 2023). On the other hand, for various compact liquid cooling systems conducting specific high Prandtl number coolants through channels with small cross-sections, the turbulent Reynolds numbers are fairly low. The associated low heat transfer rates consistently lead to higher wall-to-bulk overheat, so that the temperature-dependence of material properties becomes an issue. The present DNS study particularly investigates such conditions, assuming a representative real coolant with a molecular Prandtl number beyond $Pr_w = 50$ together with moderate Reynolds number conditions below $Re_{\tau,w} = 380$. The effect of temperature-dependent fluid properties on the turbulence statistics shall be analyzed by comparison against the corresponding results for constant material properties. For the considered setting, the variation of the density due to volumetric dilatation always remains sufficiently small, so that the effect of buoyancy forces is neglected. This will be also underpinned by the low Richardson or Rayleigh numbers presented in the discussion of the results.

2 Mathematical Formulation

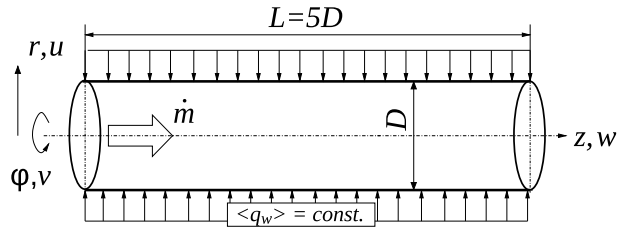
2.1 Governing Conservation Equations and Numerical Setup

The present DNS solved the incompressible conservation equations of mass, momentum, and energy in non-dimensional representation written as

$$\frac{\partial \varrho^*}{\partial t^*} + \nabla \cdot (\varrho^* \mathbf{U}^+) = 0 \quad (1)$$

$$\frac{\partial \varrho^* \mathbf{U}^+}{\partial t^*} + \nabla \cdot (\varrho^* \mathbf{U}^+ \mathbf{U}^+) = -\nabla P^+ + \nabla \cdot \left[\frac{\mu^*}{Re_{\tau,w}} \left(2\underline{S} - \frac{2}{3} tr(\underline{S}) \mathbf{I} \right) \right] + \mathbf{f}_w \quad (2)$$

Fig. 1 Computational domain



$$\frac{\partial \chi^+}{\partial t^*} + \nabla \cdot (\mathbf{U}^+ \chi^+) - \chi^+ \nabla \cdot \mathbf{U}^+ = \frac{1}{\rho^* \text{Re}_{\tau,w} \text{Pr}_w} \nabla \cdot \left(\frac{\lambda^*}{c_p^*} \nabla \chi^+ \right) + f_\chi, \quad (3)$$

respectively, using the pipe diameter D , the wall friction velocity $w_\tau = (\tau_w/\rho_w)^{1/2}$, and specific wall friction enthalpy $h_\tau = \langle q_w \rangle / \rho_w w_\tau$ as reference scales. $\langle q_w \rangle$ represents the imposed constant average wall heat flux. $\mathbf{U}^+ = \mathbf{U}/w_\tau = (u^+, v^+, w^+)^T$ and $\chi^+ = (h_w - h)/h_\tau$ represent the non-dimensional velocity vector in cylindrical coordinates ($r^* = r/D, \varphi, z^* = z/D$)^T and specific enthalpy difference to the wall value, respectively. $\underline{S} = (\nabla \mathbf{U}^+ + \nabla \mathbf{U}^{+T})/2$ denotes the rate of strain tensor. The asterisked material properties, specific heat c_p^* , thermal conductivity λ^* , molecular viscosity μ^* , and density ρ^* , always refer to the corresponding wall values. In consistence with the assumed incompressible low Mach number flow, the density is decoupled from pressure, and may therefore vary only with temperature due to volumetric dilatation. $\text{Re}_{\tau,w} = \rho_w w_\tau D / \mu_w$ and $\text{Pr}_w = \mu_w c_{p,w} / \lambda_w$ denote the Reynolds and Prandtl number based on wall reference conditions at temperature $\langle T_w \rangle$, respectively. The terms $\mathbf{f}_w = 4 \mathbf{e}_z$ and $f_\chi = w^+ / \dot{m}^*$ with $\dot{m}^* = \dot{m} / D^2 \pi \rho_w w_\tau$ arise from the enforcement of axial periodicity, assuming the flow to be driven by a constant average axial pressure gradient and heated by a constant average wall heat flux.

The conservation Eqs. (1–3) were directly solved in cylindrical coordinates, applying a 4th order accurate Finite-Volume discretization in space and a 2nd order accurate Adams-Bashforth scheme in time. The time step was dynamically adapted using a CFL number set to 0.5.

Figure 1 shows the computational domain, axially extending over five diameters. No-slip boundary conditions are prescribed for the velocity, $\mathbf{U}^+ = 0$, and a uniform time-averaged wall heat flux $\langle q_w \rangle$ with $\chi^+ = 0$ is imposed at the wall. Periodic boundary conditions are used for all flow and thermal variables in the axial direction assuming dynamically and thermally fully developed flow. In a rigorous sense, the latter assumption conflicts with the account of temperature-dependent material properties, whose average values may axially change due to the wall heating. For the considered domain length, this axial variation is, however, quantitatively well below the radial variation normal to the wall, so that it can be reasonably neglected, justifying the assumption of a fully developed flow conditions and axial periodicity.

The computational mesh consists of $256 \times 1024 \times 2048$ cells in the radial, azimuthal, and streamwise directions, respectively. For capturing the small-scale near wall structures, the mesh is clustered in the radial direction towards the solid wall and towards the center of the pipe, whereas uniform grid spacing is used in the homogeneous azimuthal and streamwise directions. The obtained grid resolution near the wall measured in wall units is $\Delta r^+ = 0.05$, $R^+ \Delta \varphi = 1.17$, and $\Delta z^+ = 0.90$.

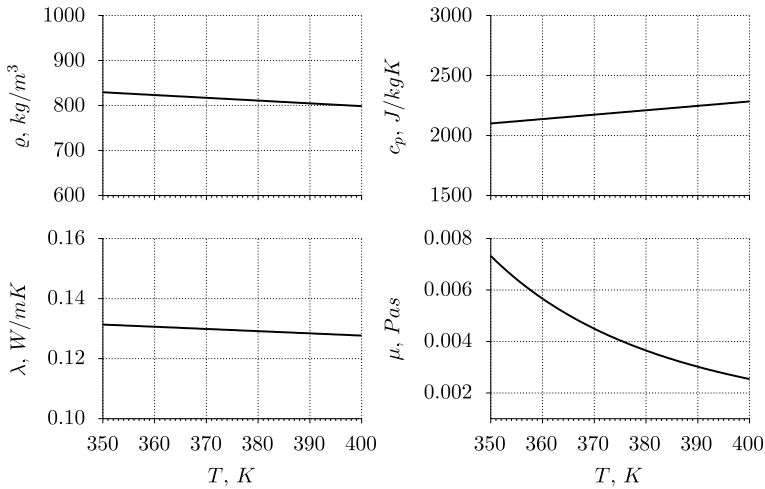


Fig. 2 Material properties versus temperature

2.2 Operating Fluid

A heat transfer oil is selected as well representative operating liquid, which is often used as a coolant in various technical applications. The variation of the material properties of the chosen oil in the considered range of temperature is shown in Fig. 2. The temperature dependence is evidently strongest for the molecular viscosity, while the other properties exhibit rather moderate changes. For the investigated thermal conditions, the presently assumed real-life oil provides the targeted range of molecular Prandtl numbers far beyond unity, being of magnitude $Pr \approx 50 \div 80$, while the spatial resolution requirements of the smallest thermal structures are computationally still feasible for DNS. The actually predicted local variation of Pr will be shown further below in the discussion of the results.

3 Results

The investigated fully developed pipe flow is specified by the friction Reynolds number $Re_{\tau,w} = 380$ and the molecular Prandtl number $Pr_w = 56$, based on the wall conditions, assuming an average wall temperature $\langle T_w \rangle = 386.0K$ as reference. The uniformly imposed average wall heat flux is $\langle q_w \rangle = 1.6 \times 10^4 W/m^2$. The chosen setting, assuming a pipe diameter $d=12mm$, produces a wall friction velocity $w_\tau = 0.1277$ m/s and a specific wall friction enthalpy $h_\tau = 151.21$ J/kg, used for the rescaling to wall units. The results for the variable and constant fluid properties are always referred to as “VFP” and “CFP”, respectively.

Figure 3 assesses the quality of the spatial resolution in terms of Kolmogorov scale $\eta = (\nu^3/\epsilon)^{1/4}$ for the dynamic turbulent structures, and the Batchelor scale $\eta_\theta = (a^2\nu/\epsilon)^{1/4} = \eta Pr^{-1/2}$ for the smallest thermal structures, where ν is the molecular kinematic viscosity, and $\epsilon = \langle \nu \partial u'_i / \partial x_j \partial u'_i / \partial x_j \rangle$ is the averaged dissipation rate of the turbulent kinetic energy. The presently used DNS grid evidently resolves the dynamic and thermal structures reasonably well over the whole cross-section. The radial variations shown here for the VFP case are quantitatively very close to, or partly lower than those presented in other

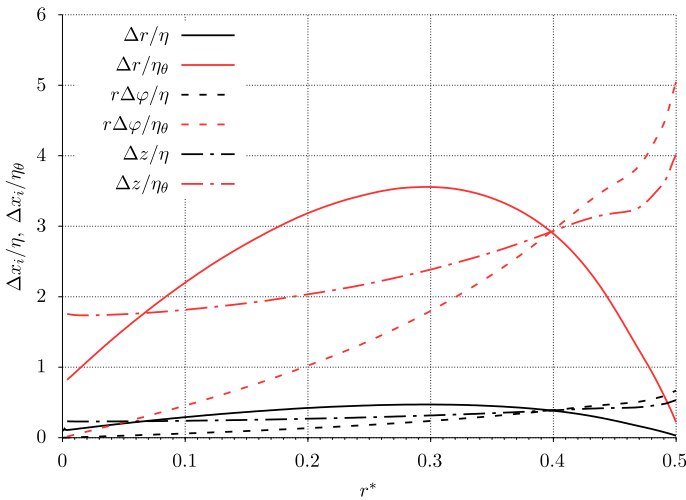


Fig. 3 Spatial resolution normalized by the Kolmogorov scale η and the smallest turbulent thermal scale η_0 versus non-dimensional radial position r^*

recent DNS studies, such as Nemati et al. (2016), Zonta et al. (2012), Lee et al. (2013), where the study with the finest resolution exhibited variations within $0.599 < \Delta y/\eta_0 < 2.98$ in wall normal, $\Delta z/\eta_0 = 7.91$ in spanwise and $\Delta x/\eta_0 = 12.4$ in streamwise direction, being well comparable to the present resolution.

4 DNS Validation

A meaningful validation against data from previous DNS in literature can be only done for the constant material property (CFP) case, as no comparable data for the presently considered particular liquid and operating conditions are available. Since the flow and thermal field are basically decoupled in the CFP case, the predicted first and second-order statistics of the velocities are validated against the widely used reference data of Wu and Moin (2008), who performed a highly resolved DNS of isothermal turbulent pipe flow at almost the same friction Reynolds number $Re_{\tau,w} = 360$. As seen from the variations over non-dimensional wall distance $y^+ = (0.5 - r^*)Re_{\tau,w}$ in Fig. 4, the agreement is excellent for the mean axial velocity, as well as for the velocity fluctuations in all directions.

Among the very scarce high-fidelity DNS data available for high molecular Prandtl numbers, the DNS of Schwertfirm and Manhart (2007) was found to match closest with the present CFP conditions. This previous study considered fully developed planar channel at comparable friction Reynolds number ($Re_{\tau,w} = 180$ based on channel half-width), including passive scalar transport in terms of mass transfer at high Schmidt numbers up to $Sc_w = 49$ with constant prescribed wall flux, which altogether can be regarded as fairly equivalent to the momentum and heat transfer conditions in the present CFP case assuming $Pr_w = 56$. As shown Fig. 5, we see again very good agreement for both the mean and fluctuations of the transported scalars. The generally a bit lower predicted profiles by Schwertfirm and Manhart (2007) are expected and reasonable, due to the, albeit small, inequality of the assumed Schmidt number and Prandtl numbers. As already indicated by the assessment

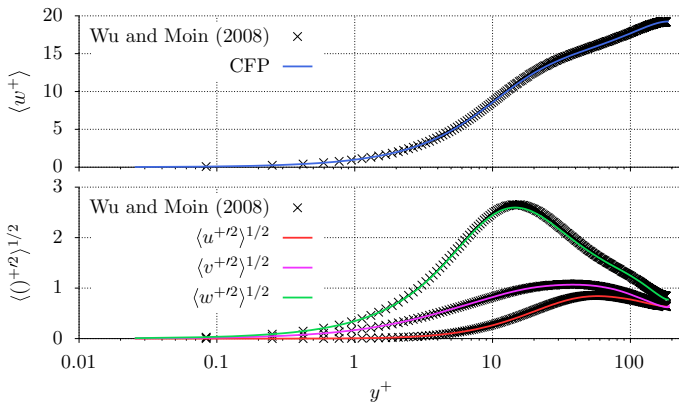


Fig. 4 Mean axial velocity and velocity rms fluctuations in radial, azimuthal, and axial direction versus wall distance y^+ for the CFP case compared against literature data

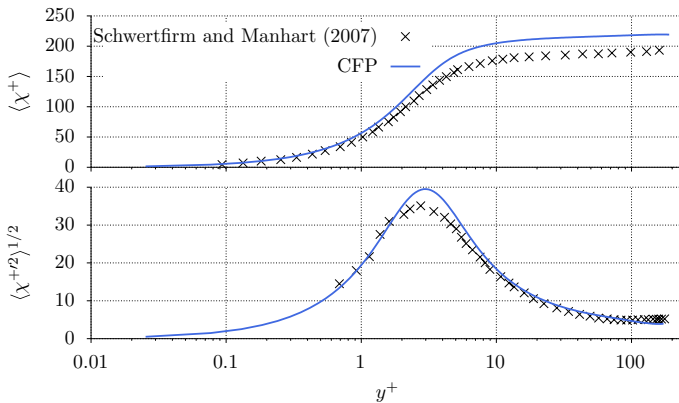


Fig. 5 Mean enthalpy and the enthalpy rms fluctuations versus y^+ for the CFP case compared against equivalent passive scalar data from literature

of the spatial resolution in Fig. 3, the validation against DNS from literature proves the present predictions as a reliable database for our analysis.

5 Turbulence Statistics

For the considered turbulent flow at a moderate Reynolds number, the tight interaction between the turbulent advective and diffusive transport of momentum and heat is strongly determined by the respective molecular transport coefficients laid down in the material properties. Their local variation in the VFP case is therefore analyzed first, discussing their radial average profiles and the therefrom derived local key parameters $\langle Re_r \rangle$ and $\langle Pr \rangle$ in Fig. 6a–c, respectively. As already anticipated by the temperature dependencies shown in Fig. 2, the dynamic viscosity quantitatively varies strongest with distance to the heated wall, while the relative changes in specific heat capacity,

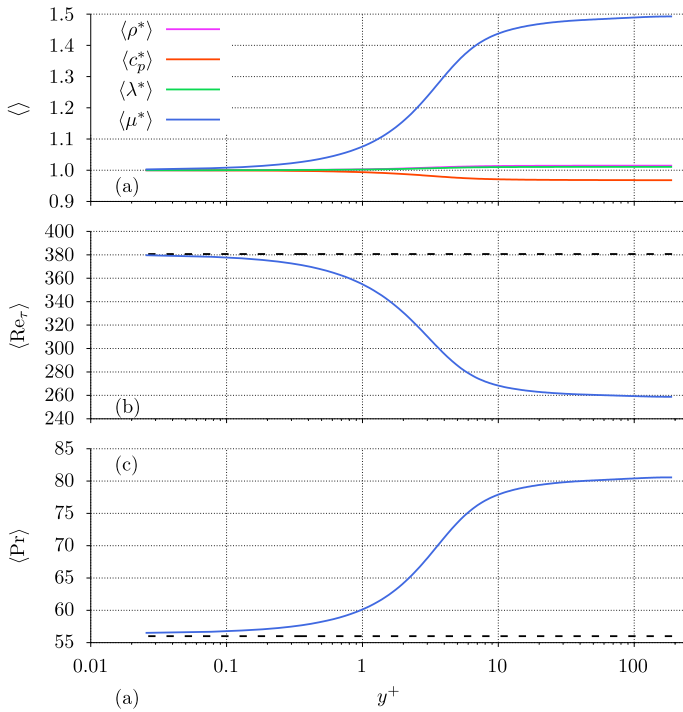


Fig. 6 **a** Average fluid properties, **b** Reynolds number, and **c** molecular Prandtl number versus wall distance y^+

density, and thermal conductivity are much smaller, almost negligible, for the two latter. As a consequence, the local Prandtl number, and, inversely, the local Reynolds number, essentially reflect the trend of the molecular viscosity, being significantly increased/decreased with wall distance, respectively. Given the insignificantly small variation of density, its turbulent fluctuations ρ^{*f} are consistently neglected in all the following statistical turbulence analyses, considering only its average values in terms of $\rho^* \approx \langle \rho^* \rangle$. The analyzed fluctuations of all flow and thermal quantities $(\)'$ are accordingly always based on Reynolds averaging with no density weighting. The very small relative change in density, being at maximum $\langle \Delta \rho^* \rangle \approx 0.01$, also translates into low friction Richardson and Rayleigh numbers. For the considered conditions they become $Ri_\tau = g \langle \Delta \rho^* \rangle D / w_\tau^2 = 0.07$ and $Ra = Ri_\tau Re_{\tau,w}^2 Pr_w = 5.8 \cdot 10^5$, which justifies the neglect of buoyancy.

The viscosity induced decrease of the local Reynolds number leads to an extensive dampening of the turbulent fluctuations of the radial and azimuthal velocity components, while the peak of the axial component is rather increased and shifted towards the center, as shown in Fig. 7. In contrast to the dampened turbulent fluctuating motion, the thermal fluctuations $\langle \chi^{*f2} \rangle^{1/2}$ are significantly enhanced, which can be attributed to the increase in the local molecular Prandtl number. The associated higher thermal conductive resistance inherently implies steeper temperature gradients, promoting the larger turbulent fluctuations in temperature seen for VFP.

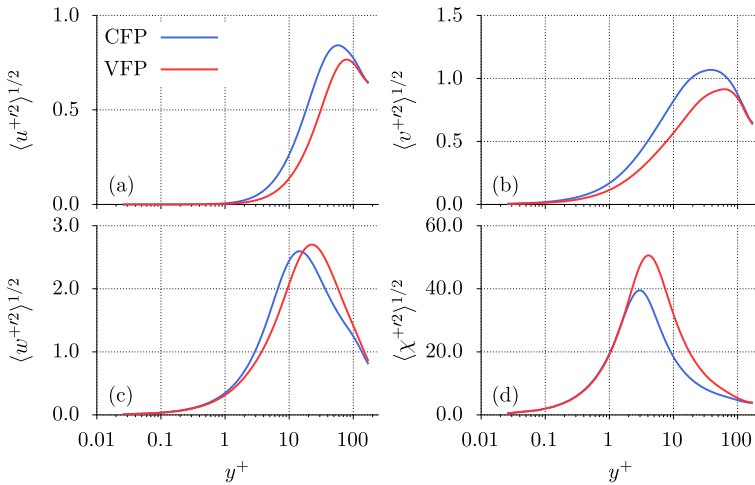


Fig. 7 Rms fluctuations of **a** radial velocity, **b** azimuthal velocity, **c** axial velocity, and **d** enthalpy versus y^+

Despite the observed opposite tendencies of the turbulent velocity and thermal fluctuations, the increased viscous dampening of the radial velocity fluctuation still dominates the turbulent components in the total flux budgets for momentum and heat, written as

$$\tau_{tot}^+ = \frac{\tau_{tot}}{\tau_w} = \tau_{lam}^+ + \tau_{turb}^+ = \langle \mu^* \rangle \frac{\partial \langle w^+ \rangle}{\partial y^+} + \phi^* \langle u^+ w^+ \rangle \tag{4}$$

$$q_{tot}^+ = \frac{q_{tot}}{\langle q_w \rangle} = q_{lam}^+ + q_{turb}^+ = \frac{1}{Pr_w} \frac{\langle \lambda^* \rangle}{\langle c_p^* \rangle} \frac{\partial \langle \chi^+ \rangle}{\partial y^+} + \phi^* \langle u^+ \chi^+ \rangle, \tag{5}$$

respectively. The non-linear components arising from turbulent fluctuations of the material properties contribute negligibly little to the diffusive fluxes, and are therefore always omitted.

As shown in Fig. 8, the turbulent contributions are always decreased near the wall, while in turn the laminar components are increased. In a parametric sense, the Reynolds number effect thus appears as predominant over the Prandtl number effect for the VFP case. The marked increase in laminar shear stress is however largely offset by the also notably increased molecular viscosity, which effectively translates into a lower shear rate near the wall, as shown in Fig. 9b. Consistent with this lower near wall gradient, the average axial velocity increases slower for VFP, remaining considerably below the profile for CFP, as seen in Fig. 9a. Further away from the hot wall region, beyond $y^+ \approx 20$, where the molecular viscosity approaches a fairly uniform bulk level, the trend is reversed and the VFP profile increases faster, which is also reflected by the larger shear rate in that region. This compensating behavior keeps the resulting bulk velocities computed from

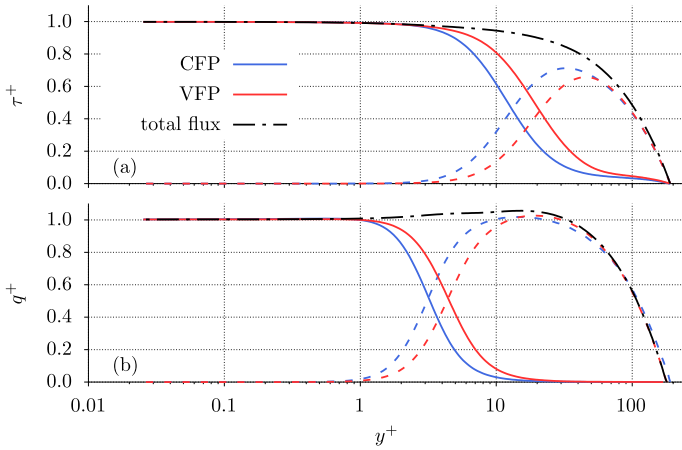


Fig. 8 Shear stress and heat flux versus wall distance y^+ : τ_{lam}^+ and q_{lam}^+ solid lines, τ_{turb}^+ and q_{turb}^+ dashed lines, τ_{tot}^+ and q_{tot}^+ dash-dotted lines

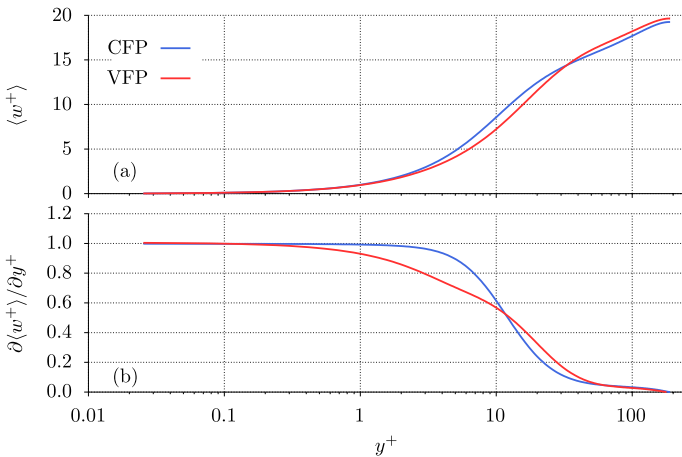


Fig. 9 **a** Mean axial velocity and **b** shear rate versus wall distance y^+

$$w_b^+ = \frac{8}{\varrho_b^*} \int_{r^*=0}^{1/2} \varrho^* \langle w^+ \rangle r^* dr^* \tag{6}$$

very close to each other, so that the resulting skin-friction coefficient obtained as

$$C_f = \frac{2}{\varrho_b^* w_b^{+2}} \tag{7}$$

only marginally changes from $C_{f,CFP} = 0.0093$ to $C_{f,VFP} = 0.0091$.

In contrast to the viscous transfer of momentum, the apparent increase of the laminar heat flux component seen in Fig. 8b almost equivalently increases the enthalpy gradient.

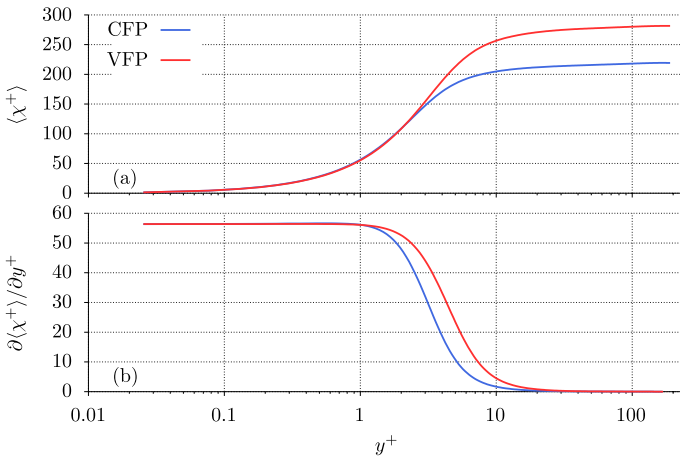


Fig. 10 **a** Mean enthalpy difference and **b** enthalpy gradient versus wall distance y^+

Unlike the molecular viscosity, the thermal conductivity remains fairly unchanged with the varying temperature, so that it does not notably compensate for the higher laminar conductive flux. Therefore, as seen from Fig. 10b, the enthalpy gradient remains consistently higher for VFP, effectively leading to higher profiles of $\langle \chi^+ \rangle$ throughout the radial domain, as seen in Fig. 10a. The consequently increased wall overhear represented by the wall-to-bulk difference obtained as

$$\chi_b^+ = \frac{8}{\rho_b^* w_b^+} \int_{r^*=0}^{1/2} \rho^* \langle w^+ \chi^+ \rangle r^* dr^* \tag{8}$$

finally produces a strongly reduced global heat transfer coefficient in terms of the Nusselt number, computed from

$$Nu = \frac{c_{p,b}^* Re_{\tau,w} Pr_w}{\chi_b^+}, \tag{9}$$

which drops from $Nu_{CFP} = 98.4$ to $Nu_{VFP} = 75.9$.

6 Turbulence Budgets

The different trends observed for VFP in the turbulent velocity fluctuations are reflected by the corresponding turbulence budgets, generally rewritten here in index notation as

$$\frac{\partial \rho^* \langle u_i^{+'} u_j^{+'} \rangle}{\partial t^*} = P_{ij}^* + C_{ij}^* + T_{ij}^* + \Pi_{ij}^* + D_{ij}^* + \epsilon_{ij}^* \tag{10}$$

with

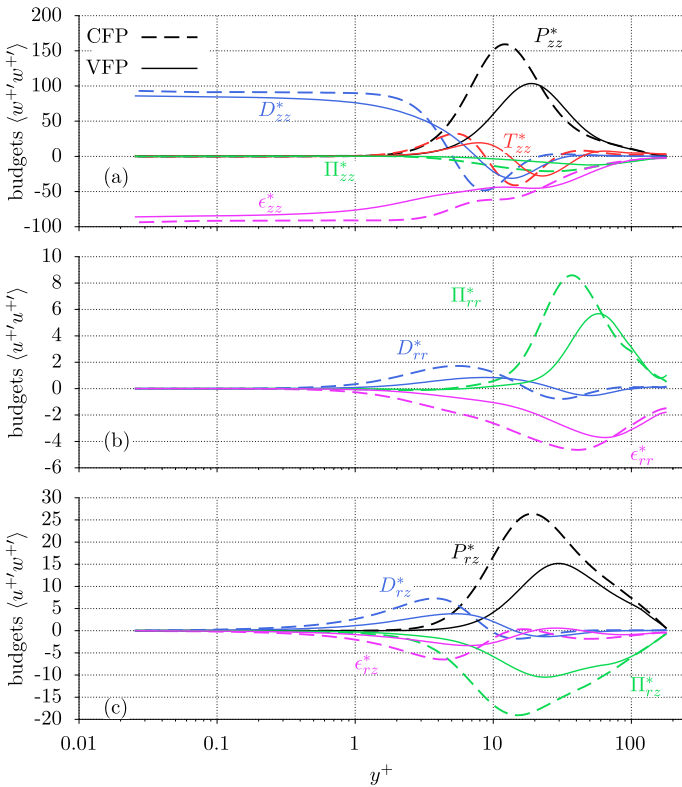


Fig. 11 Budgets of **a** $\langle w^{+'}w^{+'} \rangle$, **b** $\langle u^{+'}u^{+'} \rangle$ and **c** $\langle u^{+'}w^{+'} \rangle$

$$\begin{aligned}
 P_{ij}^* &= -\rho^* \langle u_j^{+'} u_k^{+'} \rangle \frac{\partial \langle u_i^{+'} \rangle}{\partial x_k^*} - \rho^* \langle u_i^{+'} u_k^{+'} \rangle \frac{\partial \langle u_j^{+'} \rangle}{\partial x_k^*}, \quad C_{ij}^* = -\frac{\partial \rho^* \langle u_k^{+'} \rangle \langle u_i^{+'} u_j^{+'} \rangle}{\partial x_k^*} \\
 T_{ij}^* &= -\frac{\partial \rho^* \langle u_i^{+'} u_j^{+'} u_k^{+'} \rangle}{\partial x_k^*}, \quad D_{ij}^* = \frac{\partial \langle \tau_{ik}^{+'} u_j^{+'} + \tau_{jk}^{+'} u_i^{+'} \rangle}{\partial x_k^*}, \quad \Pi_{ij}^* = -\left\langle u_i^{+'} \frac{\partial p^{+'}}{\partial x_j^*} + u_j^{+'} \frac{\partial p^{+'}}{\partial x_i^*} \right\rangle, \\
 \epsilon_{ij}^* &= -\left\langle \tau_{ik}^{+'} \frac{\partial u_j^{+'}}{\partial x_k^*} + \tau_{jk}^{+'} \frac{\partial u_i^{+'}}{\partial x_k^*} \right\rangle, \quad \tau_{mn}^{+'} = \frac{\langle \mu^* \rangle}{\text{Re}_{\epsilon,w}} \left(\frac{\partial u_m^{+'}}{\partial x_n^*} + \frac{\partial u_n^{+'}}{\partial x_m^*} \right)
 \end{aligned}$$

where, C_{ij}^* represents the mean convection, P_{ij}^* the production, T_{ij}^* the turbulent diffusion, Π_{ij}^* the velocity pressure-gradient tensor, D_{ij}^* D_{ij}^* the viscous diffusion, ϵ_{ij}^* the dissipation, and $\tau_{mn}^{+'}$ the viscous stress fluctuation tensor. Rewriting Eq. (10) for the normal axial turbulent stress $\langle w^{+'2} \rangle$, the expression for the production term reads

$$P_{zz}^* = -\rho^* \langle u^{+'} w^{+'} \rangle \frac{\partial \langle w^{+'} \rangle}{\partial y^{+'}}. \tag{11}$$

Due to the smaller turbulent fluxes, accompanied by the also lower shear rate, as already shown in Figs. 8a and 9b, respectively, P_{zz}^* remains substantially lower near the wall for VFP. Accordingly, as seen in Fig. 11a, P_{zz}^* starts increasing radially further inside, and beyond $y^+ \approx 20$, supported by a locally higher shear rate, it even exceeds the values for

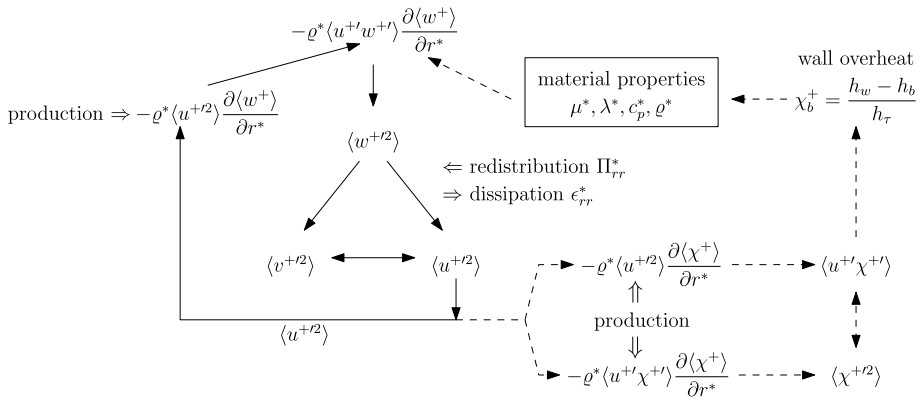


Fig. 12 Cycle of turbulence, extended by heat transfer loop for VFP (dashed paths)

CFP. A smaller proportion of the produced energy of $\langle w^{+2} \rangle$ is however, redistributed to the other normal stress components by the pressure–velocity interaction, as indicated by the significantly lower redistribution term, occurring in the budget as

$$\Pi_{zz}^* = - \left\langle 2w^{+2} \frac{\partial p^{+2}}{\partial z^*} \right\rangle$$

This weaker redistribution also explains the rise of the axial velocity fluctuation rms $\langle w^{+2} \rangle^{1/2}$ up to a peak, which is located radially further inwards and quantitatively even higher than for CFP, as seen in Fig. 7c. The pressure-strain induced steering of turbulence towards isotropy is evidently attenuated for VFP, thus keeping the turbulence more anisotropic.

Figure 11b shows the budget of radial normal stress component $\langle u^{+2} \rangle$. The redistribution based on pressure velocity interaction, which occurs here as

$$\Pi_{rr}^* = - \left\langle 2u^{+2} \frac{\partial p^{+2}}{\partial r^*} \right\rangle,$$

is evidently again notably lower for VFP over most parts of the radial domain. Since this budget inherently has no other source than the redistribution term Π_{rr}^* , this input of energy essentially taken from $\langle w^{+2} \rangle$ is considerably reduced. Accompanied by more pronounced losses associated with a comparatively stronger dissipation ϵ_{rr}^* , the resulting intensity of radial velocity fluctuations generally remain at a significantly lower level in the VFP case, as already shown in Fig. 7a. As an important consequence, the reduction of the radial velocity fluctuation u^{+2} markedly lowers the production in the budget of the turbulent shear stress $\langle u^{+2} w^{+2} \rangle$ written as

$$P_{rz}^* = - \rho^* \langle u^{+2} \rangle \frac{\partial \langle w^+ \rangle}{\partial r^*}, \tag{12}$$

and depicted in Fig. 11c. The apparent decrease in production P_{rz}^* is consistent with lower turbulent shear stress shown in Fig. 8a for VFP across the whole hot near wall region. The decrease in turbulent shear stress $\langle u^{+2} w^{+2} \rangle$ in turn translates into a lower production P_{zz}^* of axial turbulent stress, closing this way the so-called "cycle of turbulence". This schematic,

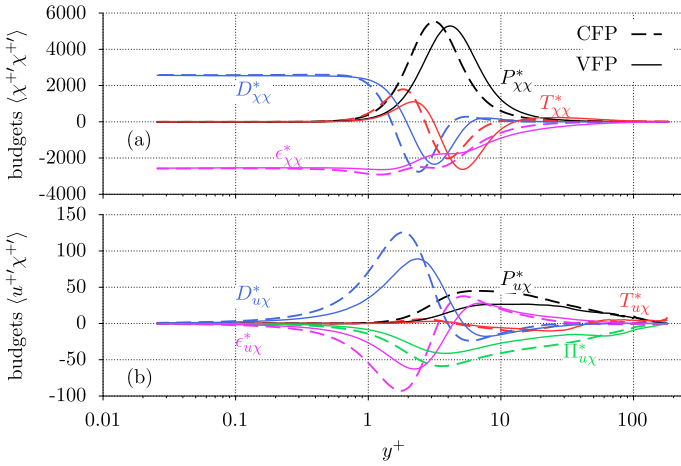


Fig. 13 Budgets of **a** $\langle \chi'^2 \rangle$ and **b** $\langle u'^i \chi'^i \rangle$

as illustrated in Fig. 12, here extended by a thermal loop relevant for the VFP case, has been originally introduced for describing the exchange of turbulent energy between the individual budgets (Leschziner 2000).

Analogously to the velocity fluctuations, the budgets of the thermal fluctuations and turbulent heat fluxes in index notation read

$$\frac{1}{2} \frac{\partial \rho^* \langle \chi'^2 \rangle}{\partial t^*} = P_{\chi}^* + C_{\chi}^* + T_{\chi}^* + D_{\chi}^* + \epsilon_{\chi}^* \tag{13}$$

with

$$P_{\chi}^* = -\rho^* \langle u_j'^+ \chi'^+ \rangle \frac{\partial \langle \chi^+ \rangle}{\partial x_j^*}, \quad C_{\chi}^* = -\frac{\partial \rho^* \langle u_j'^+ \rangle \langle \chi'^2 \rangle}{\partial x_j^*}, \quad T_{\chi}^* = -\frac{\partial \rho^* \langle u_j'^+ \chi'^{+2} \rangle}{\partial x_j^*}$$

$$D_{\chi}^* = \frac{\partial \langle q_j'^+ \chi'^+ \rangle}{\partial x_j^*}, \quad \epsilon_{\chi}^* = -\langle q_j'^+ \frac{\partial \chi'^+}{\partial x_j^*} \rangle, \quad q_j'^+ = \frac{\langle \lambda^* \rangle}{\langle c_p^* \rangle \text{Re}_{\tau,w} \text{Pr}_w} \frac{\partial \chi'^+}{\partial x_j^*}$$

and

$$\frac{\partial \rho^* \langle u_i'^+ \chi'^i \rangle}{\partial t^*} = P_{i\chi}^* + C_{i\chi}^* + T_{i\chi}^* + \Pi_{i\chi}^* + D_{i\chi}^* + \epsilon_{i\chi}^* \tag{14}$$

with

$$P_{i\chi}^* = -\rho^* \langle u_j'^+ \chi'^{+i} \rangle \frac{\partial \langle u_i^+ \rangle}{\partial x_j^*} - \rho^* \langle u_i'^+ u_j'^+ \rangle \frac{\partial \langle \chi^+ \rangle}{\partial x_j^*},$$

$$C_{i\chi}^* = \frac{\partial \rho^* \langle u_j \rangle \langle u_i'^+ \chi'^+ \rangle}{\partial x_j^*}, \quad T_{i\chi}^* = -\frac{\partial \rho^* \langle u_i'^+ u_j'^+ \chi'^+ \rangle}{\partial x_j^*}, \quad \Pi_{i\chi}^* = -\langle \chi'^+ \frac{\partial p'^+}{\partial x_i^*} \rangle,$$

$$D_{i\chi}^* = \frac{\partial \langle \tau_{ij}'^+ \chi'^+ \rangle}{\partial x_j^*} - \frac{\partial \langle q_j'^+ u_i'^+ \rangle}{\partial x_j^*}, \quad \epsilon_{i\chi}^* = -\langle \tau_{ij}'^+ \frac{\partial \chi'^+}{\partial x_j^*} \rangle - \langle q_j'^+ \frac{\partial u_i'^+}{\partial x_j^*} \rangle,$$

respectively. As seen from the budgets of $\langle \chi'^2 \rangle$ in Fig. 13, the respective production occurring as

$$P_{\chi\chi}^* = -\rho^* \langle u'^+ \chi'^+ \rangle \frac{\partial \langle \chi'^+ \rangle}{\partial r^*} \quad (15)$$

is shifted again away from the heated wall for VFP. However, due to the consistently higher enthalpy gradients, as already shown in Fig. 10b, $P_{\chi\chi}^*$ then rises up to almost the same maximum level as in the CFP case. Together with the significant increase in the local molecular Prandtl number shown in Fig. 6c, this readily explains the comparatively higher peak and increased core flow level of $\langle \chi'^2 \rangle^{1/2}$ observed for VFP in Fig. 7d.

In contrast to $P_{\chi\chi}^*$, the production in the budget of the radial turbulent heat flux, written as

$$P_{u\chi}^* = -\rho^* \langle u'^2 \rangle \frac{\partial \langle \chi'^+ \rangle}{\partial r^*}, \quad (16)$$

by definition more pronouncedly reflects the significant attenuation of u'^+ associated with VFP. Therefore, as seen from Fig. 13b, $P_{u\chi}^*$ falls mostly well below the corresponding profile of the CFP case, which finally leads to the lower radial turbulent heat flux seen near the wall for VFP in Fig. 8b. The apparently reduced heat transfer rate thus sustains the underlying attenuation of the turbulent motion, most prominently observed in the radial velocity fluctuation u'^+ . The resulting larger wall-to-bulk difference in temperature (wall overheat), as indicated by Fig. 10a, in turn translates into a higher molecular bulk viscosity, further promoting the viscous dampening of the turbulent velocity component u'^+ . The enhanced thermal fluctuations seen in Fig. 7d for VFP do not compensate for the lower u'^+ in the turbulent radial heat flux near the wall, as $\langle \chi'^2 \rangle^{1/2}$ radially peaks further inside.

The key role of the turbulent radial normal stress $\langle u'^2 \rangle$ in all involved near wall transfer processes is overviewed in the extended cycle of turbulence in Fig. 12. As the most salient feature, the increased viscous dampening of u'^+ effectively attenuates the feed back of turbulent energy to both the turbulent fluxes of momentum and heat, essentially owing to the decreased respective production terms P_{rr}^* and $P_{u\chi}^*$, as well as the higher dissipative losses ϵ_{rr}^* .

7 Conclusions

For the considered high Prandtl number working fluid and operating conditions, the strong increase in molecular viscosity with distance to the heated wall most significantly modulates the transfer processes of momentum and heat. The opposite trends of the local Reynolds and Prandtl numbers for varying temperature give rise to a marked dampening of the velocity fluctuations, especially of the radial (wall normal) component, while the thermal enthalpy fluctuations are strongly enhanced. The increase of the latter turned out as insufficient in magnitude and located radially too far inside to compensate for the strongly dampened turbulent convection near the wall, leading to a considerably smaller turbulent heat flux and Nusselt number for VFP. The effect of locally varying Reynolds number thus predominates over the effect of local Prandtl number.

In contrast to the Nusselt number, the skin friction coefficient C_f remains almost unchanged for VFP, which is due to the very different extent of dependence on the temperature of molecular viscosity and thermal conductivity. The increase in molecular viscosity largely covers the

increase of the laminar component in the budget of total shear stress, as the turbulent component is decreased. The velocity gradients remain consequently low near the wall, while the enthalpy gradients are almost equivalently increased with the higher laminar heat flux component, as the thermal conductivity does not significantly rise. The apparent different trends for momentum and heat transfer strongly question the applicability of the Reynolds analogy, which is widely assumed in standard turbulence models for relating directly the turbulent thermal diffusivity to the eddy viscosity, introducing a turbulent Prandtl number of order unity.

The attenuation of the radial turbulent velocity component strongly impacts all turbulence budgets, consistently reducing the production terms of both the turbulent momentum and heat fluxes. In the sense of a positive feedback mechanism, the lower heat transfer rate effectively sustains the viscosity induced dampening, as the effected decrease in bulk temperature inherently leads to a higher viscosity. The also attenuated redistribution of the axial turbulent stresses imply less intense steering of the turbulence towards isotropy, driven by the pressure-strain interaction. The, in consequence, more anisotropic turbulence in the radially inner region further represents a further possible challenge to turbulence modelling, assuming mostly isotropy.

Author contributions Both authors contributed equally to this work.

Funding Open access funding provided by Graz University of Technology.

Data Availability Not applicable.

Declarations

Conflict of interest The authors declare no competing interests.

Ethics Approval Not applicable.

Informed Consent Not applicable.

Open Access This article is licensed under a Creative Commons Attribution 4.0 International License, which permits use, sharing, adaptation, distribution and reproduction in any medium or format, as long as you give appropriate credit to the original author(s) and the source, provide a link to the Creative Commons licence, and indicate if changes were made. The images or other third party material in this article are included in the article's Creative Commons licence, unless indicated otherwise in a credit line to the material. If material is not included in the article's Creative Commons licence and your intended use is not permitted by statutory regulation or exceeds the permitted use, you will need to obtain permission directly from the copyright holder. To view a copy of this licence, visit <http://creativecommons.org/licenses/by/4.0/>.

References

- Alcántara-Ávila, F., Hoyas, S., Pérez-Quiles, M.J.: Direct numerical simulation of thermal channel flow for $Re_\tau = 5000$ and $Pr = 0.71$. *J. Fluid Mech.* **916**, 29 (2021)
- Boersma, B.J.: Direct numerical simulation of turbulent pipe flow up to a Reynolds number of 61,000. *J. Phys. Conf. Ser.* **318**, 042045 (2011)
- García-Villalba, M., Álamo, J.C.: Turbulence modification by stable stratification in channel flow. *Phys. Fluids* **23**(4), 045104 (2011)
- Hoyas, S., Oberlack, M., Alcántara-Ávila, F., Kraheberger, S.V., Laux, J.: Wall turbulence at high friction Reynolds numbers. *Phys. Rev. Fluids* **7**(1), 014602 (2022)
- Kawamura, H., Ohsaka, K., Abe, H., Yamamoto, K.: DNS of turbulent heat transfer in channel flow with low to medium-high Prandtl number fluid. *Int. J. Heat Fluid Flow* **19**(5), 482–491 (1998)

- Kim, J., Moin, P.: Transport of passive scalars in turbulent channel flow. Technical Memorandum 89463, National Aeronautics and Space Administration, Moffet Field, California (Sept 1987)
- Kozuka, M., Seki, Y., Kawamura, H.: DNS of turbulent heat transfer in a channel flow with a high spatial resolution. *Int. J. Heat Fluid Flow* **30**(3), 514–524 (2009)
- Lee, J., Jung, S.Y., Sung, H.J., Zaki, T.A.: Effect of wall heating on turbulent boundary layers with temperature-dependent viscosity. *J. Fluid Mech.* **726**, 196–225 (2013)
- Leschziner, M.: The computation of turbulent engineering flows with turbulence-transport closures. In: *Advanced Turbulent Flow Computations*, pp. 209–277. Springer, Udine, Italy (2000)
- Moser, R.D., Kim, J., Mansour, N.N.: Direct numerical simulation of turbulent channel flow up to $Re_\tau = 590$. *Phys. Fluids* **11**(4), 943–945 (1999)
- Na, Y., Hanratty, T.: Limiting behavior of turbulent scalar transport close to a wall. *Int. J. Heat Mass Transf.* **43**(10), 1749–1758 (2000)
- Nemati, H., Patel, A., Boersma, B.J., Pecnik, R.: The effect of thermal boundary conditions on forced convection heat transfer to fluids at supercritical pressure. *J. Fluid Mech.* **800**, 531–556 (2016)
- Patel, A., Boersma, B.J., Pecnik, R.: Scalar statistics in variable property turbulent channel flows. *Phys. Rev. Fluids* **2**(8), 084604 (2017)
- Patel, A., Peeters, J.W., Boersma, B.J., Pecnik, R.: Semi-local scaling and turbulence modulation in variable property turbulent channel flows. *Phys. Fluids* **27**(9), 095101 (2015)
- Piller, M.: Direct numerical simulation of turbulent forced convection in a pipe. *Int. J. Numer. Meth. Fluids* **49**(6), 583–602 (2005)
- Pirozzoli, S., Romero, J., Fatica, M., Verzicco, R., Orlandi, P.: DNS of passive scalars in turbulent pipe flow. *J. Fluid Mech.* **940**, 45 (2022)
- Redjem-Saad, L., Ould-Rouiss, M., Lauriat, G.: Direct numerical simulation of turbulent heat transfer in pipe flows: Effect of prandtl number. *Int. J. Heat Fluid Flow* **28**(5), 847–861 (2007)
- Scagliarini, A., Einarsson, H., Gylfason, A., Toschi, F.: Law of the wall in an unstably stratified turbulent channel flow. *J. Fluid Mech.* **781**, 5 (2015)
- Schwertfirm, F., Manhart, M.: DNS of passive scalar transport in turbulent channel flow at high Schmidt numbers. *Int. J. Heat Fluid Flow* **28**(6), 1204–1214 (2007)
- Tiselj, I., Bergant, R., Mavko, B., Bajisic, I., Hetsroni, G.: DNS of turbulent heat transfer of channel flow with heat conduction in solid wall. *ASME J. Heat Transf.* **123**, 849–857 (2001)
- Wu, X., Moin, P.: A direct numerical simulation study on the mean velocity characteristics in turbulent pipe flow. *J. Fluid Mech.* **608**, 81–112 (2008)
- Yao, J., Rezaeiravesh, S., Schlatter, P., Hussain, F.: Direct numerical simulations of turbulent pipe flow up to $Re_\tau \approx 5200$. *J. Fluid Mech.* **956**, 18 (2023)
- Zonta, F., Marchioli, C., Soldati, A.: Modulation of turbulence in forced convection by temperature-dependent viscosity. *J. Fluid Mech.* **697**, 150–174 (2012)
- Zonta, F., Soldati, A.: Stably stratified wall-bounded turbulence. *Appl. Mech. Rev.* **70**(4), 040801 (2018)